ROYAL SOCIETY OF CHEMISTRY

PAPER

Check for updates

One-step additive manufacturing of Ni–Mn–Sn alloys with a large elastocaloric effect†

Wen Sun,[abc] Hanyang Qian,[ab] Qi Fu,[d] Mingxiao Zhang,[abg] Juan Cheng,[e] Zhaojun Mo, [ID][d] Jian Liu,[f] Wei Li[g] and Guowei Li [ID] *[ab]

Ni–Mn–Sn metamagnetic shape memory alloys have garnered significant attention in solid-state refrigeration due to their highly tunable magnetic properties and large elastocaloric effects. However, their intrinsic brittleness hinders practical application. Laser powder bed fusion (L-PBF) additive manufacturing technology can overcome the machining difficulties of brittle alloys, enabling freeform geometrical design. Meanwhile, the rapidly cooled melt pool also facilitates the attainment of austenite functional phases. However, the elastocaloric effect of L-PBF alloys, especially for directly printed bulk materials without heat treatment, has not been systematically studied in Ni–Mn-based alloys. This work successfully obtained a rapidly solidified microstructure with austenite phases in $Ni_{45}Mn_{44}Sn_{11}$ alloys using a one-step L-PBF method without heat treatment. The relative densities of the L-PBF samples reached a maximum of 98.20%, with the entropy change values remaining stable in the range of 26 to 31 J kg^{-1} K^{-1}. Compared to compression along the building direction, impressive and larger elastocaloric temperature changes (6.7 K) were achieved when compressing along the scanning direction due to the dominance of columnar grains and micron-sized defects. A maximum entropy change of 4.8 J kg^{-1} K^{-1} is achieved under an external magnetic change of 5 T. This work offers a simplified method for rapidly constructing solid-state refrigeration alloys with a large elastocaloric effect.

Introduction

Heusler-type Ni–Mn–X (X = Sn, Ga, In and Sb) metamagnetic shape memory alloys have been extensively studied owing to their multifunctional properties, *e.g.* magnetostrain, magnetoresistance effect, considerable electrocatalytic activity and caloric effects.[1–3] Caloric effects can be exceptionally efficient forms of energy conversion.[4] The solid-state refrigeration based on the magnetocaloric, elastocaloric, barocaloric or multicaloric effect[5–8] is regarded as a promising environmentally friendly alternative to vapor compression refrigeration.[9–12] Fundamentally, the caloric effect originates from the martensitic transformation from a high-temperature phase to a low-temperature phase with different structures in shape memory alloys.[13–15] Therefore, the volume fraction of martensitic transformation affects the values of isothermal entropy change (ΔS) or adiabatic temperature change (ΔT_{ad}). For Ni–Mn–Sn alloys, the high-temperature phase typically exists in the forms of the $L2_1$ phase (bcc structure), γ phase (fcc structure), $D0_3$ phase (X_3Y prototype) and D_{19} phase (hexagonal structure).[16–19] Only the $L2_1$ cubic phase could transform into the martensite phase, therefore the $L2_1$ phase serves as the functional phase for refrigeration. Accordingly, reducing the fraction of those non-functional phases is advantageous for enhancing the caloric effect. A thermal treatment method is commonly employed to eliminate non-functional phases in Ni–Mn-based alloys prepared by conventional preparation methods such as arc melting, induction melting, directional solidification, *etc.* Advantageously, the non-functional phase can be effectively inhibited by rapid solidified technology, for example, the austenite phase has been directly obtained in melt-spun Ni–Mn-based ribbons at high rotational speeds.[20,21] Interestingly, laser powder bed fusion (L-PBF), as a common technology in additive manufacturing (AM), also features extremely fast heating and cooling ramps ($\sim 10^6$ K s^{-1}).[22–24] It becomes an effective method to obtain rapid solidification microstructures. Meanwhile, AM overcomes the machining

[a] *CAS Key Laboratory of Magnetic Materials, Ningbo Institute of Materials Technology and Engineering, Chinese Academy of Sciences (CAS), Ningbo 315201, China. E-mail: liguowei@nimte.ac.cn*

[b] *University of Chinese Academy of Sciences, Beijing 100049, China*

[c] *Key Laboratory of Advanced Marine Materials, Ningbo Institute of Materials Technology and Engineering, CAS, China*

[d] *Key Laboratory of Rare Earths, Ganjiang Innovation Academy, CAS, Ganzhou 341119, China*

[e] *State Key Laboratory of Baiyunbo Rare Earth Resource Researches and Comprehensive Utilization, Baotou Research Institute of Rare Earths, Baotou, 0472, China*

[f] *School of Materials Science and Engineering, Shanghai University, Shanghai 200444, China*

[g] *CISRI & NIMTE Joint Innovation Center for Rare Earth Permanent Magnets, NIMTE, CAS, China*

† Electronic supplementary information (ESI) available: Experimental section, Fig. S1–S15 and Tables S1–S3. See DOI: https://doi.org/10.1039/d4tc02734e

difficulties in brittle alloy systems and provides an approach to realize geometric freedom.[25–29]

For elastocaloric and magnetocaloric refrigeration prototypes, the refrigerant requires high surface area structures such as honeycomb, riverbed and fin structures.[30,31] For the Ni–Mn-based Heusler alloys with intrinsic brittleness and poor machining properties, the fabrication of sophisticated geometries *via* conventional methods remains challenging.[32–34] The AM is suitable for preparing Ni–Mn-based alloys with high surface area structures and functional phases. Several works have been reported on 3D-printed Ni–Mn–Sn(Ga)-based alloys. Rittinghaus *et al.*[35] manufactured $Ni_{47.2}Mn_{39.2}Sn_{13.0}$ alloys by electron beam powder bed fusion (E-PBF) and L-PBF. The alloys of L-PBF and E-PBF indicated a magnetic entropy change of 3.95 J kg^{-1} K^{-1} under an external field change of 5.0 T. Sun *et al.*[36] developed manufacturing routes for $Ni_{50}Mn_{37}Sn_{13}$ alloys using the L-PBF technique by in situ alloying from elemental constituents, and the maximum value of magnetic entropy change is about 0.5 J kg^{-1} K^{-1} under a field change of 1.0 T. The L-PBF $Ni_{40}Mn_{43}Sn_{11}Co_6$ alloys had a maximum magnetic entropy change of about 14 J kg^{-1} K^{-1} under an external field change of 5.0 T.[37] The $Ni_{49.5}Mn_{19.1}Cu_{6.6}Ga_{24.8}$ alloy with 1.2 K hysteresis was prepared by powder bed binder jet 3D printing with subsequent sintering and the maximum magnetic entropy change was about 12.0 J kg^{-1} K^{-1} at 2 T.[38] These works focus on the microstructure, magnetic properties and magnetocaloric effect, and most properties are obtained through heat treatment. Elastocaloric cooling has been identified as the highest promising alternative to vapor-compression technology in room temperature refrigeration applications,[39,40] while the elastocaloric effect of 3D-printed materials has rarely been investigated. Recently, we reported the elastocaloric effect of $Ni_{45}Mn_{44}Sn_{11}$ alloys *via* L-PBF after annealing, and a large adiabatic temperature change (ΔT_{ad}) of 11 K has been achieved.[41] Unfortunately, L-PBF alloys inevitably exhibit cracks and void defects.[36,37,41] It is crucial to investigate the influence of defects on mechanical properties and elastocaloric effects. In this work, the austenite phase is directly obtained *via* a rapid scanning strategy of 1000–3000 mm s^{-1} in L-PBF, meanwhile, the alloy exhibits a significant elastocaloric effect without heat treatment. The formation mechanism of defects in the alloy was explored. The influence of microstructures and defects on the mechanical properties and elastocaloric effects was investigated.

Methods

The powders with a nominal composition of $Ni_{45}Mn_{44}Sn_{11}$ (element atomic %) were prepared by gas atomization, and 4 wt% extra Mn was added to the raw materials to compensate for Mn volatilization. Powders in the size range of 15–53 μm for printing were sieved by standard sieves. The powder size distribution for printing was analyzed using a Microtrac S3500 tri-laser diffraction particle analyzer. The L-PBF samples were fabricated under an argon atmosphere using a BLT-A300 system (BRIGHT LASER TECHNOLOGIES, China). The different combinations of L-PBF parameters were selected as shown in Table S1 (ESI†). The corresponding laser energy density (E) is calculated using the equation[42] $E = P/(\nu \times H \times d)$, where P is the laser power, ν is the scanning speed, H is the hatching spacing and d is the layer thickness. Two P/ν ratios were chosen in order to theoretically maintain an E of 25 J mm^{-3} or 30 J mm^{-3}. The applied energy density was selected based on our previous L-PBF works on Ni–Mn–Sn alloys.[41]

The microstructure of the samples was examined using scanning electron microscopy (SEM, FEI Quanta FEG 250) and Zeiss Imager M2m optical microscopy. An energy dispersive spectrometer (EDS) was utilized to analyze the distribution of elements. The elemental contents of the samples were measured using an inductively coupled plasma optical emission spectrometer (ICP-OES, SPECTRO ARCOS). Each sample was prepared in duplicate for testing, and the element concentrations presented in Table S2 (ESI†) are the average values. To evaluate the defects of samples, 3D X-ray tomography scanning was performed using a ZEISS Xradia Context micro-CT system (Micro-CT, METROTOM 160 kV) with a voxel size of 1.99 μm. Texture analyses were performed *via* electron backscatter diffraction (EBSD, OXFORD Nordlys Max2). All inverse pole figures (IPFs) were defined such that the ⟨001⟩ direction is aligned with the scanning direction. The phase identification was performed using an X-ray diffractometer (XRD, Bruker D8) with Cu Kα radiation. The characteristic temperatures of martensitic transformation (M_s, M_f, A_s, A_f) and latent heats (ΔH) were determined using differential scanning calorimetry (DSC, NETZSCH DSC 214) with a heating/cooling rate of 10 K min^{-1}, where M_s/M_f and A_s/A_f are the martensitic transformation start/finish temperature and austenite transformation start/finish temperature, respectively. The ΔS in a thermally induced martensitic transformation was determined as $\Delta S = \Delta H/T_0$, where $T_0 = (M_s + A_f)/2$ is the equilibrium temperature. A differential thermal analysis (DTA) was employed to measure the energy changes of the P_{150} sample in a higher temperature range with a heating/cooling rate of 10 K min^{-1}.

The mechanical test specimens were cut from the L-PBF alloys into pieces with dimensions of 3.5 × 3.5 × 7 mm^3. The compressive experiment was conducted on a universal testing machine (SUNs-UTM 5000). A low strain rate of 0.000071 s^{-1} was used to ensure the isothermal conditions upon loading, while a high strain rate of 0.048 s^{-1} was used to approach the adiabatic conditions upon unloading. The control mode required the strain magnitude, which was measured using an extensometer. The loading strain is gradually increased at 0.5% strain step until the sample fracture. The temperature change associated with the elastocaloric effect was monitored using an infrared thermometer (FLIR, A325sc) during unloading. Magnetization *vs.* temperature (*M–T*) and magnetization *vs.* field (*M–H*) curves were measured using a superconducting quantum interference device vibrating sample magnetometer (SQUID-VSM).

Results and discussion

The Ni–Mn–Sn powders for AM were obtained through the argon gas atomization process. The XRD pattern of the as-prepared

This journal is © The Royal Society of Chemistry 2024

J. Mater. Chem. C, 2024, **12**, 16864–16871 | **16865**

powder and the corresponding Rietveld refinement indicate good agreement between the experimental data and the calculated structure based on the L2$_1$ structure of Ni$_2$MnSn (Fig. 1a). The EDS results indicate that the average chemical composition of the powder is Ni$_{43.56}$Mn$_{45.03}$Sn$_{11.42}$ (element atomic %) as shown in Fig. S1 (ESI†). We further used ICP-OES to verify the compositions of the samples. The ICP-OES results indicate that the average chemical composition of the powder is Ni$_{43.88}$Mn$_{43.79}$Sn$_{12.33}$ (at%) as shown in Table S2 (ESI†), which is close to the EDS results. The sieved powder exhibits a narrow Gaussian-type particle size distribution (Fig. 1b), with over 90% (D90) of the particles measuring below 48.1 μm in size. The well-defined spherical shape and narrow size distribution of the powders are ideal for constructing elastocaloric devices using the AM strategy.

By adjusting the laser energy density and scanning speed, a series of L-PBF Ni–Mn–Sn alloys with dimensions of 15 × 15 × 20 mm^3 were produced at different laser powers ranging from 50 to 180 W (Fig. 1c). To achieve rapidly solidified microstructures, high scanning rates (1000–3000 mm s^{-1}) are employed. The backscattered SEM images indicate high homogeneity in the constructed samples without secondary phases (Fig. 1d and Fig. S2, ESI†). The EDS also suggests a homogeneous distribution of the elemental composition (Fig. S3, ESI†). The average chemical composition of P$_{50}$ is Ni$_{44.53}$Mn$_{42.81}$Sn$_{12.66}$ (at%) as shown in Table S2 (ESI†). Compared to the composition of the powder, the reduction in Mn content is due to the slight evaporation of Mn elements after laser remelting. Micron-sized cracks and pores are observed on the surface when the laser power is below 180 W, with the cracks spreading along the building direction (BD).
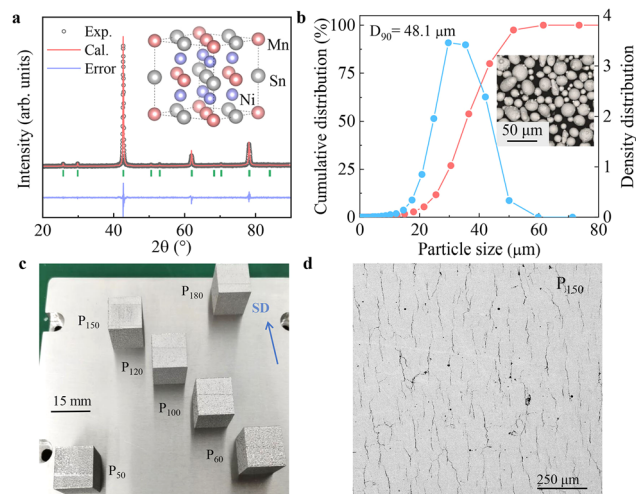
The XRD patterns of the constructed samples are shown in Fig. 2a. All the main diffraction peaks can be indexed to the single cubic L2$_1$ crystal structure austenite phase. Only a tiny peak corresponding to the martensitic phase is observed, suggesting the high phase purity of the samples. This is because the rapid solidification of the melt pool during the L-PBF process could effectively suppress the formation of D0$_3$ phases and γ phases, which are commonly observed during equilibrium solidification. To further verify that there are no D0$_3$ phases and γ phases in the sample, the DTA was employed to measure energy changes at higher temperatures as shown in Fig. S4 (ESI†). Besides the exothermic/endothermic peaks associated with melting/solidification, no phase transition peaks of a second phase were observed.

Now we start to investigate the elastocaloric effect of the L-PBF samples by tracking the thermally driven martensitic phase transformation processes. Differential scanning calorimetry (DSC) curves of L-PBF Ni–Mn–Sn samples constructed at different laser powers are displayed in Fig. 2b and Fig. S5 (ESI†). The exothermic and endothermic peaks can be attributed to the phase transformation between martensitic and austenitic phases, which are in good agreement with previous studies in Ni–Mn–Sn Heusler compounds.[43] It is interesting to observe that the endothermic/exothermic peaks are nearly identical for P$_{60}$–P$_{150}$ samples in Fig. 2b and Fig. S5 (ESI†), implying that the well-defined martensitic transformation is not sensitive to changes in laser power from 60–150 W. The robustness of the L-PBF strategy is further confirmed by the almost unchanged average characteristic temperatures of martensitic transformation ($T_M = (M_s + M_f + A_s + A_f)/4$) in P$_{60}$–P$_{150}$ samples, which can be determined by measuring the starting and finishing temperatures for austenite and martensite (Fig. S6, ESI†). The relatively high T_M for the sample constructed under 180 W is due to the large laser power, which leads to the evaporation of Mn elements during the manufacturing process. As expected, the Mn content decreases from 42.52 at% to 41.78 at%, when the laser power is increased from 150 to 180 W (Table S2, ESI†). This decrease in Mn content causes the transition temperatures to shift towards higher values.[16] The isothermal entropy changes (ΔS) are obtained from the enthalpy changes (ΔH) and characteristic temperatures of martensitic transformation (Fig. 2c and Fig. S6, ESI†). The values of ΔS remain stable within the range of 26 ∼ 31 J kg^{-1} K^{-1}, which are significantly higher than Ni–Mn–Cu–Ga (Sn),[19,51] Ni–Fe–Co–Mn–Sn[44] and Ni–Mn–Sn–Pd.[52] This fully demonstrates the high reliability of AM in the preparation of refrigeration materials. The stress–strain curves were obtained through isothermal stress loading and adiabatic stress unloading at a temperature of 300.5 K (Fig. 2d and Fig. S7, ESI†). The loading strain was gradually increased in steps of 0.5% until the sample fractured. The corresponding temperature change, ΔT_{ad}, represents the average temperature change measured using an infrared thermal imager (Fig. S8, ESI†). The stress–strain curve exhibits a notably steep transformation plateau, likely due to inconsistent critical stresses for martensitic phase transformation caused by complex microstructures and residual internal stresses. The stress–strain curves demonstrate complete reversibility when the applied
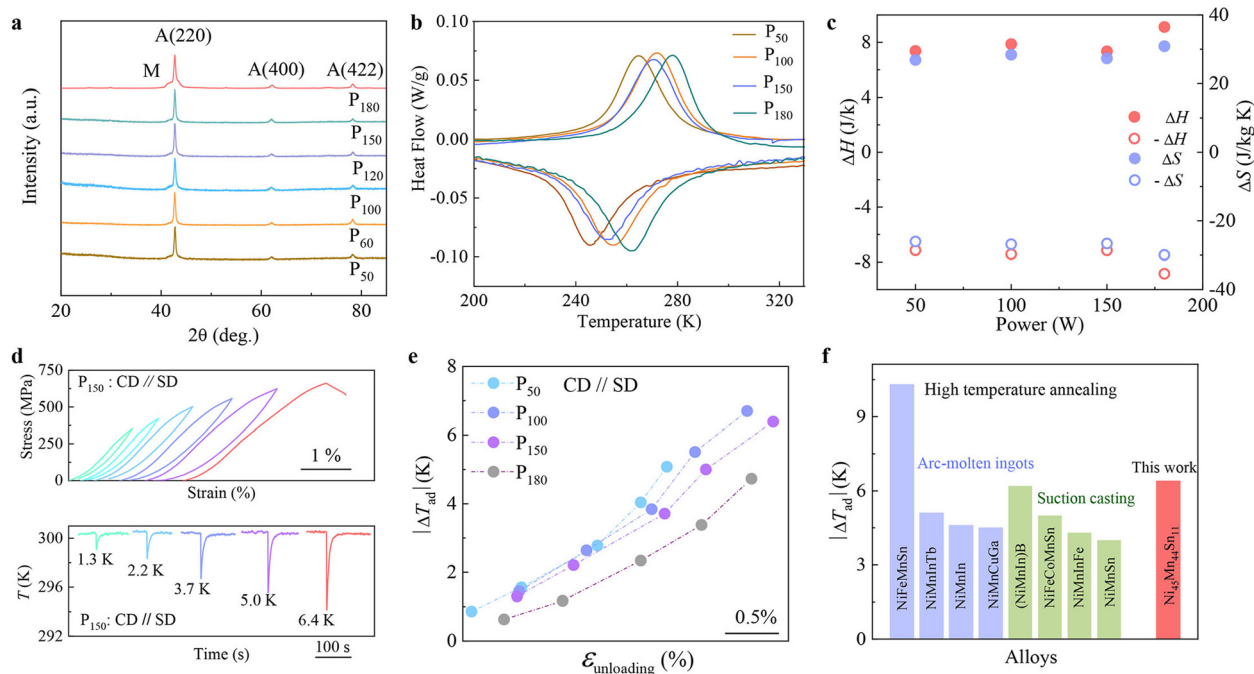

Fig. 1 (a) XRD pattern and the corresponding Rietveld refinement in powders. The internal inset shows the bcc unit cell structure of the L2$_1$ austenite phase. (b) Powder diameter distribution curve (red) and cumulative diameter distribution curve (blue). The internal image shows a SEM morphology of the powder. (c) 3D printed samples with length, width, and height of 15 × 15 × 20 mm^3. The samples with different laser powers have been labeled, and the scanning direction (SD) has been marked with arrows. (d) Backscattered SEM microstructures are perpendicular to the SD in the P$_{150}$ sample.

16866 | J. Mater. Chem. C, 2024, **12**, 16864–16871

This journal is © The Royal Society of Chemistry 2024

Fig. 2 (a) XRD patterns of the L-PBF samples at room temperature. The diffraction peaks corresponding to austenite (A) and martensite (M). (b) DSC curves of alloys, (c) enthalpy change (ΔH) and entropy change (ΔS) of samples prepared *via* different laser powers. (d) Stress–strain curves at room temperature under compression along SD (CD//SD), and corresponding temperature-time curves upon unloading in the P_{150} sample. (e) The values of adiabatic temperature change (ΔT_{ad}) with different unloading strains ($\varepsilon_{unloading}$) when compressed along the SD. (f) Comparison of ΔT_{ad} for typical room-temperature elastocaloric materials prepared by arc-molten and suction casting.[43–50]

strain is less than 2% (Fig. 2d). However, residual strain appears after unloading when the applied strain exceeds 3%. A residual strain of about 0.3% was observed after loading to 3% strain, and then unloading along the SD direction. Although the residual strain increases with increasing compressive strain, the amount of increase in residual strain is less than that of the compressive strain. As a result, more martensite transforms to austenite during rapid unloading, leading to an increase in elastocaloric temperature changes with increasing unloading strain ($\varepsilon_{unloading}$) as shown in Fig. 2e. Temperature changes ranging from 4.7 to 6.7 K were observed after compression along the SD in samples P_{50}–P_{180}. We further compared the mechanical properties and elastocaloric effects during compression along the BD direction (Fig. S7 and S8, ESI†). When loaded parallel to the BD direction, the strain reached only 2% before the sample fractured. The ΔT_{ad} values ranged from 2.0 to 4.0 K due to the smaller unloading strain compared to compression along the SD direction. We compare the elastocaloric effects of the L-PBF Ni–Mn–Sn alloys with that of samples obtained through arc melting and sintering.[43–50] The elastocaloric performance surpasses that of most heat-treated samples prepared by arc melting and suction casting, such as $Ni_{50}Mn_{34}In_{15.6}Tb_{0.4}$,[46] $Ni_{50}Mn_{34.8}In_{15.2}$,[47] $Ni_{50}Mn_{18.5}Cu_{6.5}Ga_{25}$,[48] $(Ni_{51.5}Mn_{33}In_{15.5})_{99.7}B_{0.3}$,[49] $Ni_{42.5}Fe_{1.0}Co_{6.5}$-$Mn_{39.5}Sn_{10.5}$,[44] $Ni_{49.9}Mn_{41.3}In_{8.8}Fe_6$[50] and $Ni_{45}Mn_{44}Sn_{11}$[43] (Fig. 2f). Our approach requires only one step to achieve a large elastocaloric temperature change in bulk alloys without heat treatment in Ni–Mn-based alloys. This method simplifies experimental procedures and improves preparation efficiency, providing a new alternative for further investigations of shape memory alloys.

Now, we aim to understand the impressive elastocaloric temperature changes achieved with this one-step L-PBF strategy. The grain morphologies were investigated using the lattice parameters of the powders. The austenite grain morphology varies across different planes. Elongated grains are observed in the building-transverse direction (BD-TD) and building-scanning direction (BD-SD) planes (Fig. 3a and Fig. S9, ESI†). Combining the alternately arranged equiaxed and columnar crystals in the TD-SD plane (Fig. 3b), it can be inferred that the predominant grains in the sample grow as platy and elongated grains along the building direction. The inverse pole figure shows a low intensity of texture, indicating a weak ⟨001⟩ texture along the SD and BD (Fig. 3c). The presence of columnar grains with preferred orientation can significantly enhance the deformation consistency of the alloy during compression along the BD and SD simultaneously. Therefore, it enables significant ΔT_{ad} during compression along the BD and SD. Additionally, compressing along the SD can effectively suppress grain boundary cracking compared to compression along the BD due to straight grain boundaries with poor intergranular cohesion. This results in higher mechanical performance and a greater elastocaloric effect when compressed along the SD (Fig. 3d).

The elastocaloric effect is closely related not only to phase constitution, grain morphology- and preferred orientation, but also to microstructures and defects. Therefore, the distribution of cracks and pores in the L-PBF samples was analyzed using micro-CT. Cracks are the main defects for all the L-PBF alloys (Fig. 3e and Fig. S10, ESI†). The cracks are categorized into
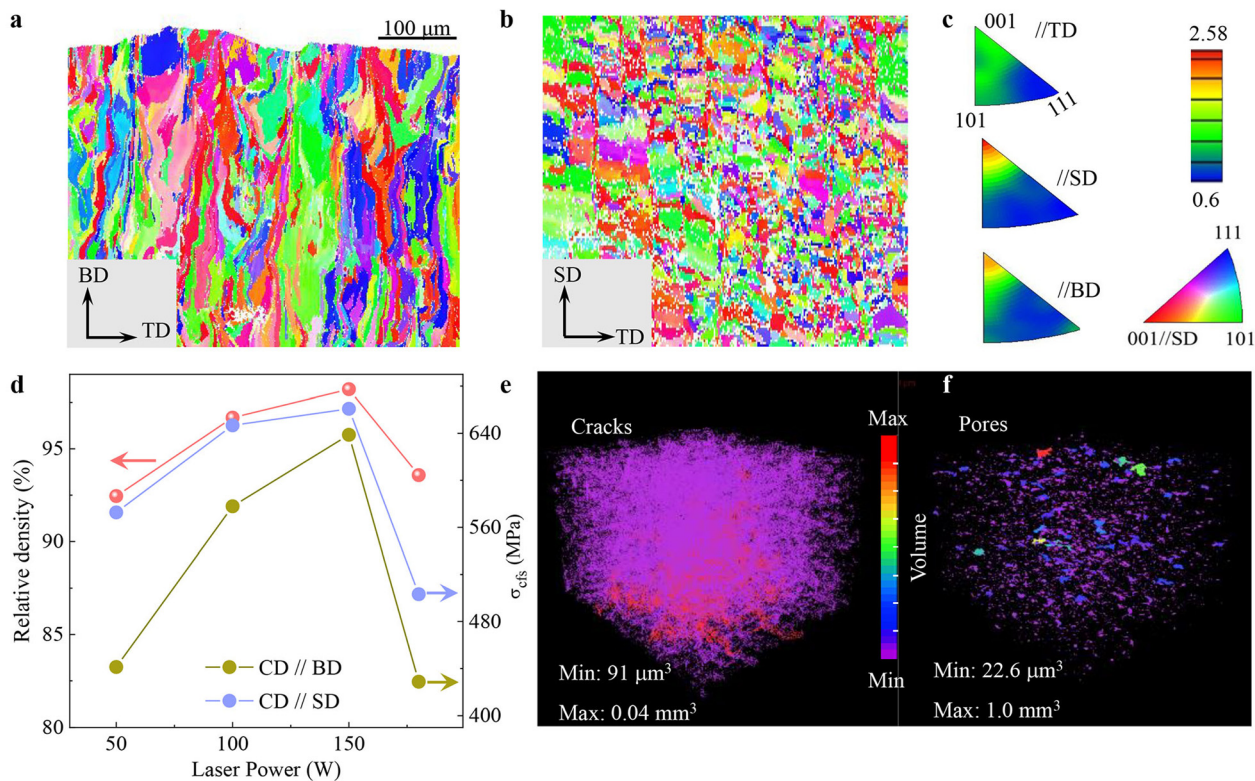
This journal is © The Royal Society of Chemistry 2024

J. Mater. Chem. C, 2024, **12**, 16864–16871 | **16867**

Fig. 3 EBSD mapping of sample P_{180} in the (a) building-transverse direction (BD-TD) and (b) transverse-scanning direction (TD-SD) planes. (c) The inverse pole figures show $\langle 001 \rangle$ texture along the SD and BD. All the inverse pole figures are plotted with the $\langle 001 \rangle$ directions parallel to the SD. (d) Relative density and fracture stress after cycling loading (σ_{cfs}) in L-PBF Ni–Mn–Sn alloys prepared with different laser powers. 3D reconstructed morphology of cracks (e) and pores (f) via Mico-CT in P_{150} samples. The different colors represent the difference in the volume of cracks and pores.

millimeter-sized cracks (highlighted in red) and micron-sized cracks (purple/blue). Information on the volume and number of cracks is summarized in Table S3 (ESI†). More than 99.9% of the cracks are micron-sized, and importantly, they are discontinuous within the L-PBF alloys. The morphology of the pores is shown in Fig. 3f and Fig. S11 (ESI†), with most of them being below 50 μm^3 (Fig. S12, ESI†). The predominance of micrometer-sized cracks and pore defects is crucial for achieving high relative densities and maintaining good mechanical properties during the compression process. Plessis et al.[53] studied the impact of pore defects on the mechanical properties in AM Ti_6Al_4V alloys. They found that fractures almost always occur at the largest pores (millimeter-sized pores), and the size of the pores is negatively correlated with yield strength and ductility. In this work, most of the defects are micron-sized cracks and voids, therefore high relative densities are achieved for most of the L-PBF samples. As shown in Table S1 (ESI†), the relative density of P_{60}–P_{150} samples is over 95%. The density of 98.20% was achieved in the samples with a laser power of 150 W and a scanning speed of 3000 mm s^{-1}. As expected, the cyclic fracture stresses (σ_{cfs}) positively correlate with the relative densities, illustrating that samples with fewer defects can withstand greater loading stress. Additionally, the σ_{cfs} along the SD are greater than those along the BD. This is because most of the columnar grains grow along the BD using a linear scanning strategy. It should be noted that the laser power

should be neither too low (below 50 W) nor too high (above 180 W). Otherwise, millimeter-sized cracks and pores will dominate the defects, leading to low relative density and detrimental effects on the mechanical properties and elastocaloric effect. A larger elastocaloric effect of 6.7/6.4 K was achieved in P_{100}/P_{150} samples compared with P_{50}/P_{180} samples (5.1/4.7 K) as shown in Fig. S8 (ESI†).

Finally, the underlying reasons for the appearance of cracks and pores are explored to optimize the microstructures and enhance elastocaloric performance in future work. Perpendicular to the SD plane, a fish scale-shaped melt pool was observed, as shown in Fig. S13 (ESI†). This wide melt pool morphology is caused by low laser energy density.[54] Meanwhile, cracks extend along the building direction in the central region of the melt pool, exhibiting a typical solidification crack morphology. A thin liquid film forms during the final stages of solidification in the central region of the weld pool. At this point, the liquid film is unable to resist the shrinkage stress during solidification, leading to rupture.[55] The cracks were also observed in other areas of the sample as shown in Fig. 4a. The distribution of crystalline orientation on both sides of the crack is calculated using the Euler angle diagram (Fig. 4b). The grain orientation difference exceeds 50° on both sides of the crack along Line 1, indicating that the crack follows the direction of the crystal boundary. In contrast, the deviation angle is less than 1° between the two sides of the crack along Line 2, indicating that the crack is an
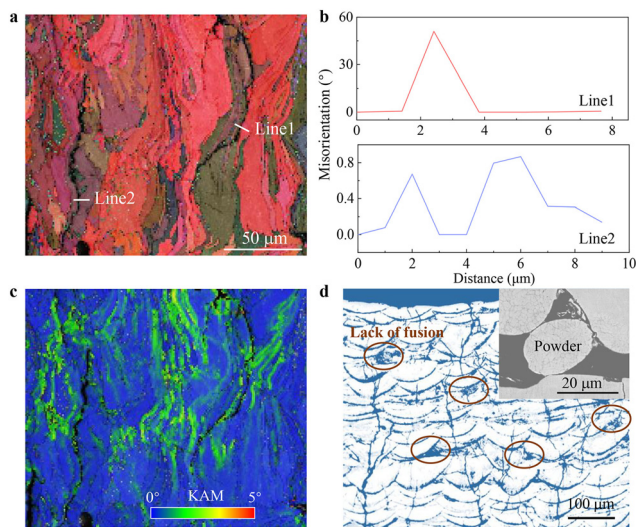
16868 | J. Mater. Chem. C, 2024, 12, 16864–16871

This journal is © The Royal Society of Chemistry 2024

Fig. 4 (a) EBSD Euler diagram. (b) The difference in grain orientation between the two sides of the cracks through Line 1 and Line 2 in Fig. 4a. (c) KAM image corresponding to the EBSD Euler diagram demonstrates the distribution of residual stress. (d) The optical microscope image of melt pools in the P_{50} sample. The inset image shows a SEM image of pores due to un-melted powders.

intragranular microcrack. Fig. 4c shows the kernel average misorientation (KAM) map which correlates with the accumulation of residual stress. The high KAM values are detected around creaks, and thereby cold cracks primarily develop in an intragranular fracture mode along the columnar grains, caused by the accumulation of residual internal stress during solidification.[56]

The pore morphology was investigated by optical microscopy and SEM. Millimeter-sized pores in the P_{50} sample appear between two adjacent laser passes (Fig. 4d). Some unmelted particles survived in the pores (the inset of Fig. 4d), as the low laser energy causes insufficient overlap of the melt pools. A large number of spherical gas pores are observed in all samples (Fig. S14a, ESI†). The gas pore morphology is characterized by small size, no un-melted particles and regular shape. The pore defects with sharp boundaries were observed in P_{180} samples. There are irregular particles in the pores (Fig. S14b, ESI†) resulting from the spattering of metal solutions. The large pores are caused by high laser power-producing spray particles, and randomly distributed pore defects are formed around the particles. These large un-melted pores are detrimental to mechanical performance. We thus proposed suppressing the un-melted void defects, and gas pore defects should also have a narrow size distribution in AM elastocaloric components. In addition, further refinement of the preparation process, such as the scanning strategy, laser energy density and scan spacing, is necessary to achieve microstructures with stronger textures in columnar grains, lower internal stresses and fewer defects.

Ni–Mn-based alloys suffer from poor cyclic stability, which is a common challenge for intermetallic compounds. Recently, various strategies have been employed to improve the cyclic stability of alloys, such as texturing polycrystals,[57] precipitating

toughening secondary phases at grain boundaries,[58] refining grains to strengthen grain boundaries[59] and precipitating nanoscale phases.[60] Laser powder bed fusion AM technology features extremely fast heating and cooling ramps ($\sim 10^6$ K s^{-1}).[23] Through the preparation process and compositional control, it is possible to simultaneously achieve microstructures with texture, fine grains and nanocrystals, thereby enhancing the cyclic stability of elastocaloric effects in 3D-printed components. Enhancing the cyclic stability of alloys using AM technology has been reported in the Ni–Ti alloy system. Hou et al.[61] designed a NiTi/Ni$_3$Ti nanocomposite structure using AM technology, enabling the printed NiTi alloy to maintain an adiabatic temperature change of 4.1 K after over 1 million cycles. Although the numerous crack defects observed in this work may significantly affect the cyclic stability of elastocaloric effects, it is anticipated that later adjustments in composition and preparation processes to avoid cracks while designing microstructures will be a feasible approach to enhance the cyclic stability of AM Ni–Mn-based components.

L-PBF Ni–Mn–Sn alloys also exhibit magnetocaloric effects. The magnetic entropy change (ΔS_M) of the AM Ni–Mn–Sn sample was calculated from the isothermal magnetization data using the Maxwell relation[62] $\Delta S_M = \mu_0 \int_0^H \left(\frac{\partial M}{\partial T} \right)_H dH$, where M, H, T and $\partial M/\partial T$ are the magnetization, magnetic-field strength, temperature and temperature derivative of magnetization, respectively. Fig. S15a (ESI†) shows the temperature dependence of magnetization. During cooling below T_C (286 K), a martensitic phase transformation occurs simultaneously with changes in magnetic properties. A 5 T magnetic field drives the phase transition temperature to shift 5 K to lower temperatures. The maximum value of ΔS_M is 4.8 J kg^{-1} K^{-1} in a field change of 5 T, as shown in Fig. S15c (ESI†). We compared the magnetocaloric effects of rapidly solidified samples obtained through direct 3D-printed and melt-spinning methods. The ΔS_M of the 3D-printed samples without heat treatment is smaller than that of the annealed melt-spun samples (7.2 J kg^{-1} K^{-1}) in a field change of 5 T for Ni$_{45}$Mn$_{44}$Sn$_{11}$ alloys.[63] The thermal hysteresis is 14 K as shown in Fig. S15a (ESI†). The magnetic hysteresis between field-up and field-down processes is also observed in isothermal magnetization curves as shown in Fig. S15b (ESI†). Gottschall et al.[6] designed a multicaloric system by combining stress fields and magnetic fields in series using the thermal hysteresis characteristics of Heusler alloys. This system effectively reduced the volume of the magnet and improved the mass ratio of the magnetocaloric material to the permanent magnet. The magnetocaloric, elastocaloric and thermal hysteresis characteristics of the L-PBF samples are advantageous for multicaloric refrigeration system applications.

Conclusions

In summary, Ni–Mn–Sn alloys with a large elastocaloric effect were directly obtained by rapid solidification in additive manufacturing. By utilizing a rapid scanning strategy, the austenite phase is directly obtained, and platy and elongated grains grow

This journal is © The Royal Society of Chemistry 2024

J. Mater. Chem. C, 2024, **12**, 16864–16871 | **16869**

along the building direction. A density of 98.20% was achieved in the samples with a laser power of 150 W and a scanning speed of 3000 mm s^{-1}. The values of entropy change remained stable in the range of 26 to 31 J kg^{-1} K^{-1}. When compressing samples perpendicular to the length direction of grains, more austenite is transformed into martensite compared to compressing samples parallel to the length direction. This results in a larger elastocaloric temperature change of 4.7 to 6.7 K upon unloading. Additionally, the predominance of micrometer-sized cracks and pore defects is crucial for achieving high relative densities and maintaining good mechanical properties during the compression process. A maximum entropy change of 4.8 J kg^{-1} K^{-1} is achieved under the external field change of 5 T. This work confirms the feasibility of directly obtaining functional phases by controlling the preparation parameters of additive manufacturing.

Author contributions

Wen Sun: data curation, investigation, methodology, validation, writing – original draft; Hanyang Qian: formal analysis, writing – review & editing; Qi Fu: formal analysis, writing – review & editing; Mingxiao Zhang: formal analysis, writing – review & editing; Juan Cheng: writing – review & editing; Zhaojun Mo: writing – review & editing; Jian Liu: writing – review & editing; Wei Li: writing – review & editing; Guowei Li: formal analysis, conceptualization, supervision, writing – review & editing.

Data availability

The data supporting this article have been included as part of the ESI.†

Conflicts of interest

There are no conflicts to declare.

Notes and references

1 R. Kainuma, Y. Imano, W. Ito, Y. Sutou, H. Morito, S. Okamoto, O. Kitakami, K. Oikawa, A. Fujita and T. Kanomata, *Nature*, 2006, **439**, 957–960.

2 L. Mañosa and A. Planes, *Adv. Mater.*, 2017, **29**, 1603607.

3 T. Kojima, S. Kameoka, S. Fujii, S. Ueda and A.-P. Tsai, *Sci. Adv.*, 2018, **4**, eaat6063.

4 V. K. Pecharsky, J. Cui and D. D. Johnson, Philosophical Transactions of the Royal Society A: Mathematical, *Phys. Eng. Sci.*, 2016, **374**, 20150305.

5 O. Gutfleisch, M. A. Willard, E. Bruck, C. H. Chen, S. G. Sankar and J. P. Liu, *Adv. Mater.*, 2011, **23**, 821–842.

6 T. Gottschall, A. Gracia-Condal, M. Fries, A. Taubel, L. Pfeuffer, L. Manosa, A. Planes, K. P. Skokov and O. Gutfleisch, *Nat. Mater.*, 2018, **17**, 929–934.

7 C. Chluba, W. Ge, R. Lima de Miranda, J. Strobel, L. Kienle, E. Quandt and M. Wuttig, *Science*, 2015, **348**, 1004–1007.

8 J. Liu, *Innovations Mater.*, 2023, **1**, 100031.

9 A. Greco, C. Aprea, A. Maiorino and C. Masselli, *Int. J. Refrig.*, 2019, **106**, 66–88.

10 B. Li, Y. Kawakita, S. Ohira-Kawamura, T. Sugahara, H. Wang, J. Wang, Y. Chen, S. I. Kawaguchi, S. Kawaguchi and K. Ohara, *Nature*, 2019, **567**, 506–510.

11 X. Moya and N. Mathur, *Science*, 2020, **370**, 797–803.

12 C. Romero-Muñiz, J. Y. Law, J. Revuelta-Losada, L. M. Moreno-Ramírez and V. Franco, *Innovations Mater.*, 2023, **1**, 100045.

13 L. Mañosa, A. Planes and M. Acet, *J. Mater. Chem. A*, 2013, **1**, 4925–4936.

14 R. Wang, S. L. Fang, Y. C. Xiao, E. L. Gao, N. Jiang, Y. W. Li and L. L. Mou, *Science*, 2019, **366**, 216–221.

15 K. Zhang, C. Tan, E. Guo, Z. Feng, J. Zhu, Y. Tong and W. Cai, *J. Mater. Chem. C*, 2018, **6**, 5228–5238.

16 Y. Murakami, Y. Watanabe, T. Kanaizuka and S. Kachi, *Trans. Jpn. Inst. Met.*, 1981, **22**, 551–557.

17 A. Pérez-Sierra, J. Pons, R. Santamarta, P. Vermaut and P. Ochin, *Acta Mater.*, 2015, **93**, 164–174.

18 B. Eggert, A. Çakır, D. Günzing, N. Josten, F. Scheibel, R. A. Brand, M. Farle, M. Acet, H. Wende and K. Ollefs, *RSC Adv.*, 2023, **13**, 18217–18222.

19 X. Zhang, H. Qian, R. Cai, Z. Wei, J. He, M. Zhang, W. Sun, J. Liu, C. Felser and G. Li, *ACS Appl. Elect. Mater.*, 2024, **6**, 4440–4448.

20 T. Bachaga, H. Rekik, M. Krifa, J. Sunol and M. Khitouni, *J. Therm. Anal. Calorim.*, 2016, **126**, 1463–1468.

21 B. Hernando, J. S. Llamazares, J. Santos, M. Sánchez, L. Escoda, J. Suñol, R. Varga, C. García and J. González, *J. Magn. Magn. Mater.*, 2009, **321**, 763–768.

22 R. R. Sélo, S. Catchpole-Smith, I. Maskery, I. Ashcroft and C. Tuck, *Addit. Manuf.*, 2020, **34**, 101214.

23 J. H. Martin, B. D. Yahata, J. M. Hundley, J. A. Mayer, T. A. Schaedler and T. M. Pollock, *Nature*, 2017, **549**, 365–369.

24 J. Ren, Y. Zhang, D. Zhao, Y. Chen, S. Guan, Y. Liu, L. Liu, S. Peng, F. Kong and J. D. Poplawsky, *Nature*, 2022, **608**, 62–68.

25 H. Wu, Y. Ren, J. Ren, L. Liang, R. Li, Q. Fang, A. Cai, Q. Shan, Y. Tian and I. Baker, *J. Alloys Compd.*, 2021, **873**, 159823.

26 H. Hou, E. Simsek, T. Ma, N. S. Johnson, S. Qian, C. Cissé, D. Stasak, N. Al Hasan, L. Zhou and Y. Hwang, *Science*, 2019, **366**, 1116–1121.

27 C. Panwisawas, Y. T. Tang and R. C. Reed, *Nat. Commun.*, 2020, **11**, 2327.

16870 | *J. Mater. Chem. C*, 2024, **12**, 16864–16871

This journal is © The Royal Society of Chemistry 2024

28 A. E.-M. A. Mohamed, M. Jeong, R. S. Sheridan and M. M. Attallah, *Addit. Manuf.*, 2022, **51**, 102620.

29 W. Sun, M. Zhang, Q. Fu, Z. Li, Z. Mo and G. Li, *Innovations Mater.*, 2023, **1**, 100032.

30 V. Sharma, L. Balderson, R. Heo, O. Bishop, C. S. M. Hunt, E. E. Carpenter, R. L. Hadimani, H. Zhao and R. Barua, *J. Alloys Compd.*, 2022, **920**, 159821.

31 C. Zhang, S. Wang, J. Li, Y. Zhu, T. Peng and H. Yang, *Innovations Mater.*, 2020, **36**, 101490.

32 K. Ahn, *J. Alloys Compd.*, 2024, **978**, 173378.

33 S. Ma, X. Zhang, G. Zheng, M. Qian and L. Geng, *Materials*, 2023, **16**, 5725.

34 G. Li, L. Xu and Z. Cao, *J. Mater. Chem. C*, 2023, **11**, 6173–6182.

35 S.-K. Rittinghaus, H. Shokri, N. Shkodich, E. Bruder, M. Farle and B. Gökce, *Addit. Manuf. Lett.*, 2023, **7**, 100159.

36 K. Sun, A. E.-M. A. Mohamed, S. Li, M. Jeong, J. Head and M. M. Attallah, *Addit. Manuf.*, 2023, **69**, 103536.

37 S. Zhong, M. Qian, J. Zhang, Q. Zhang, L. Sun, P. Shen, X. Zhang and L. Geng, *Addit. Manuf.*, 2024, **79**, 103941.

38 E. Stevens, K. Kimes, D. Salazar, A. Mostafaei, R. Rodriguez, A. Acierno, P. Lazpita, V. Chernenko and M. Chmielus, *Addit. Manuf.*, 2021, **37**, 10.

39 W. Goetzler, R. Zogg, J. Young and C. Johnson, Navigant Consulting Inc., prepared for US Department of Energy, 2014, vol. 199.

40 S. Qian, D. Catalini, J. Muehlbauer, B. Liu, H. Mevada, H. Hou, Y. Hwang, R. Radermacher and I. Takeuchi, *Science*, 2023, **380**, 722–727.

41 W. Sun, X. Lu, Z. Wei, Q. Li, Z. Li, Y. Zhang and J. Liu, *Addit. Manuf.*, 2022, **59**, 103125.

42 V. Laitinen, A. Salminen and K. Ullakko, *J. Laser Appl.*, 2019, **31**, 022303.

43 W. Sun, J. Liu, B. Lu, Y. Li and A. Yan, *Scripta Mater.*, 2016, **114**, 1–4.

44 Y. Qu, A. Gracia-Condal, L. Manosa, A. Planes, D. Cong, Z. Nie, Y. Ren and Y. Wang, *Acta Mater.*, 2019, **177**, 46–55.

45 Y. Zhu, H. Xuan, J. Su, F. Chen, K. Zhang, P. Han and J. Qiao, *Phys. Lett. A*, 2022, **451**, 128374.

46 Q. Shen, D. Zhao, W. Sun, Y. Li and J. Liu, *J. Alloys Compd.*, 2017, **696**, 538–542.

47 X.-M. Huang, L.-D. Wang, H.-X. Liu, H.-L. Yan, N. Jia, B. Yang, Z.-B. Li, Y.-D. Zhang, C. Esling, X. Zhao and L. Zuo, *Intermetallics*, 2019, **113**, 106579.

48 F. Villa, E. Bestetti, R. Frigerio, M. Caimi, C. Tomasi, F. Passaretti and E. Villa, *Materials*, 2022, **15**, 7123.

49 Z. Yang, D. Cong, X. Sun, Z. Nie and Y. Wang, *Acta Mater.*, 2017, **127**, 33–42.

50 J. L. Lukas Pfeuffer, Navid Shayanfar, Stefan Riegg, David Koch, Andreas Taubel, Franziska Scheibel, Nagaarjhuna A. Kani, Esmaeil Adabifiroozjaei, L. Molina-Luna, K. Skokov and O. Gutfleisch, *Acta Mater.*, 2021, **221**, 117390.

51 E. Villa, C. Tomasi, A. Nespoli, F. Passaretti, G. Lamura and F. Canepa, *J. Mater. Res. Technol.*, 2020, **9**, 2259–2266.

52 A. Wederni, M. Ipatov, E. Pineda, L. Escoda, J.-M. González, M. Khitouni and J.-J. Suñol, *Processes*, 2020, **8**, 1582.

53 A. Du Plessis, I. Yadroitsava, S. G. Le Roux, I. Yadroitsev, J. Fieres, C. Reinhart and P. Rossouw, *J. Alloys Compd.*, 2017, **724**, 267–274.

54 J. Mei, Y. Han, J. Sun, M. Jiang, G. Zu, X. Song, W. Zhu and X. Ran, *J. Alloys Compd.*, 2024, **981**, 173623.

55 A. Mostafaei, C. Zhao, Y. He, S. R. Ghiaasiaan, B. Shi, S. Shao, N. Shamsaei, Z. Wu, N. Kouraytem and T. Sun, *Curr. Opin. Solid State Mater. Sci.*, 2022, **26**, 100974.

56 Q. Wei, Y. Xie, Q. Teng, M. Shen, S. Sun and C. Cai, *Chin. J. Mech. Eng.*, 2022, **1**, 100055.

57 L. Wei, X. Zhang, J. Liu and L. Geng, *AIP Adv.*, 2018, **8**, 055312.

58 H. Qian, R. Cai, X. Lu, W. Sun, G. Li, Z. Wei and J. Liu, *Mater. Design*, 2024, **244**, 113162.

59 Z. Yang, D. Cong, Y. Yuan, Y. Wu, Z. Nie, R. Li and Y. Wang, *Mater. Res. Lett.*, 2019, **7**, 137–144.

60 J. Xuan, J. Gao, Z. Ding, X. Li and J. Zhu, *J. Alloys Compd.*, 2021, **877**, 160296.

61 E. S. Huilong Hou, T. Ma, N. S. Johnson, S. Qian, C. Cissé, D. Stasak, N. Al Hasan, L. Zhou, Y. Hwang, R. Radermacher, V. I. Levitas, M. J. Kramer, M. A. Zaeem, A. P. Stebner, R. T. Ott, J. Cui and I. Takeuchi, *Science*, 2019, **366**, 1116–1121.

62 B. Shen, J. Sun, F. Hu, H. Zhang and Z. Cheng, *Adv. Mater.*, 2009, **21**, 4545–4564.

63 T. Chabri, A. Venimadhav and T. Nath, *J. Magn. Magn. Mater.*, 2018, **466**, 385–392.

This journal is © The Royal Society of Chemistry 2024

J. Mater. Chem. C, 2024, **12**, 16864–16871 | **16871**